

PAPER

Cite this: *RSC Adv.*, 2016, 6, 82743

A series of BiO_xI_y/GO photocatalysts: synthesis, characterization, activity, and mechanism†

 Shang-Yi Chou,^a Wen-Hsin Chung,^b Li-Wen Chen,^a Yong-Ming Dai,^a Wan-Yu Lin,^b Jia-Hao Lin^a and Chiing-Chang Chen^{*a}

A series of bismuth oxyiodide (BiO_xI_y)-grafted graphene oxide (GO) sheets with different GO contents were synthesized through a simple hydrothermal method. This is the first report where four composites of BiOI/GO, Bi₄O₅I₂/GO, Bi₇O₉I₃/GO, and Bi₅O₇I/GO have been characterized using X-ray diffraction, transmission electron microscopy, scanning electron microscopy energy-dispersive spectroscopy, Fourier transform infrared spectroscopy, X-ray photoelectron spectroscopy, and diffuse reflectance spectroscopy. The assembled BiO_xI_y/GO composites exhibited excellent photocatalytic activities in the degradation of crystal violet (CV) under visible light irradiation. The order of rate constants was as follows: Bi₇O₉I₃/GO > Bi₄O₅I₂/GO > Bi₄O₅I₂ > Bi₇O₉I₃ > Bi₅O₇I/GO > BiOI/GO > BiOI > Bi₅O₇I > GO. The photocatalytic activity of the Bi₇O₉I₃/GO (or Bi₄O₅I₂/GO) composite reached a maximum rate constant of 0.351 (or 0.322) h⁻¹, which was 1.8 (or 1.7) times higher than that of Bi₇O₉I₃ (or Bi₄O₅I₂), 6–7 times higher than that of BiOI/GO, and 119–130 times higher than that of BiOI. The quenching effects of different scavengers and electron paramagnetic resonance demonstrated that the superoxide radical (O₂⁻) played a major role and holes (h⁺) and hydroxyl radicals ([•]OH) played a minor role as active species in the degradation of crystal violet (CV) and salicylic acid (SA). Possible photodegradation mechanisms are proposed and discussed in this research.

 Received 13th May 2016
Accepted 17th August 2016

DOI: 10.1039/c6ra12482h

www.rsc.org/advances

1. Introduction

Triarylmethane (TAM) dyes have been used as colorants in industry and as antimicrobial agents.¹ A recent report demonstrated that they might also be supplied as targetable sensitizers in the photodestruction of specific cellular components.² The binding of CV to DNA is probably ionic, as opposed to intercalative; and it binds stably to double-stranded DNA, and when converted to a colorless carbinol form it is used for assessing the binding of other molecules to DNA.³ However, great concerns have been expressed about the thyroid peroxidase-catalyzed oxidation of the TAM class of dyes because the reaction might produce various *N*-dealkylated primary and secondary aminobenzenes, with structures similar to those of aminobenzene carcinogens.⁴

In recent years, semiconductor photocatalysis driven by visible light has sparked significant research interest because it provides a promising mechanism for solving energy supply and environmental pollution problems. An environmentally cheap

and powerful photocatalyst is an important constituent for practical applications of photocatalysis.⁵ The photocatalytic degradation of CV dyes has been researched using several systems to determine active species, including bismuth oxyhalide,^{6–8} TiO₂,⁹ PbBiO₂Br/BiOBr,¹⁰ Bi₂WO₆,¹¹ BaTiO₃,¹² and ZnO.¹³

Recently, the study of visible light-driven photocatalysts has attracted considerable attention as an alternative for the elimination of toxic materials from wastewater. An effective and simple tactic for improving the photocatalytic activity of a photocatalyst is the incorporation of a heterostructure because hetero-composites have great potential for tuning the desired electronic properties of photocatalysts and efficiently separating photo-formed electron-hole pairs.^{14,15}

In recent years, as a new family of advantageous photocatalysts, bismuth oxyhalides^{16–18} have demonstrated unusual photocatalytic activities because their unique layered structure features an internal static electric field vertical in each layer that may occasion more effective separation of photo-formed charge carriers. Bismuth oxyiodides have received increased interest because of their suitable energy gaps, stability, and relatively superior photocatalytic activities.^{19–22}

Because the valence band for bismuth oxyiodides contains mostly O_{2p} and I_{5p} orbitals, whereas the conduction band is based on the Bi_{6p} orbital,²³ iodine-poor bismuth oxyiodides could be illustrated to have band-gap energies higher than

^aDepartment of Science Education and Application, National Taichung University of Education, Taichung 403, Taiwan. E-mail: ccchen@mail.ntcu.edu.tw; Fax: +886-4-2218-3560; Tel: +886-4-2218-3406

^bDepartment of Plant Pathology, National Chung Hsing University, Taichung 402, Taiwan

† Electronic supplementary information (ESI) available. See DOI: 10.1039/c6ra12482h

Table 1 Photocatalytic properties of bismuth oxyiodide/GO nanocomposite photocatalysts under visible light irradiation

Composite photocatalyst	Mass fraction of GO	Parameters of photocatalytic experiments	Photocatalytic activity	Reference photocatalyst/ photocatalytic activity	Enhancement factor	Reference
BiOI/GO	1.2%	Phenol	55% decomposition in 2.5 h	GO: 0% BiOI: 40%	— 1.4	66
Bi ₇ O ₉ I ₃ /rGO	10%	Rhodamine B	95.8% in 100 min 78.5% in 150 min	Bi ₇ O ₉ I ₃ : 74.7% rGO: 0%	— 2.13	67
		Phenol		rGO: 0% Bi ₇ O ₉ I ₃ : 49.2%	— 2.29	
BiOI/rGO	0.5%	Methyl orange	99% in 3 h.	rGO BiOI: 46%	— 2.15	68
BiOI/GR	5%	Rhodamine B	80% in 4 h.	GR: 0% BiOI: 11%	— 7.3	69
BiOI/GR	2%	Methyl orange	88.0% in 4 h.	GR: 0% BiOI: 27.6%	— 6.0	70

those of BiOI but lower than those of Bi₂O₃;^{24,25} hence, these materials might be used as visible light-responsive photocatalysts. In particular, the structure and composition of bismuth oxyiodides strongly influence their electronic, optical, oxidizing abilities, and other physicochemical properties, giving an opportunity to acquire novel photocatalysts for effective degradation of environmental and toxic pollutants. However, the synthesis methods, characterization, and evaluated properties of a series of bismuth oxyiodides have remained rare until recently.

In the past several years, graphene (GR) has drawn attention because of its remarkable properties.^{26,27} According to a previous report, the theoretical specific surface area of GR is 2630 m² g⁻¹.^{26,27} Therefore, it can be used as an ideal support material with improved interfacial contact and enhanced adsorption activity. GR has a powerful but flexible structure with a high carrier mobility. Thus, a GR-based hybrid photocatalyst will show excellent photocatalytic efficiency. Furthermore, it can be easily produced from graphite, which is cheap and naturally abundant. Currently, many studies have reported that the integration of GR and a semiconductor photocatalyst, such as TiO₂,²⁸ Ag/Ag₂CO₃,²⁹ Bi_{3.64}Mo_{0.36}O_{6.55},³⁰ and ZnO,³¹ could form hybrid materials with superior photocatalytic activity. For example, Trapalis *et al.*³² revealed that TiO₂-graphene composites prepared through a solvothermal process displayed improved photocatalytic performance in removing NO_x compared with pure commercial TiO₂.

GR or reduced graphene oxide (rGO) are suitable candidates because of the high electron mobility (>15 000 cm² V⁻¹ s⁻¹) and the flexible sheet nature that is beneficial for supporting photocatalysts. A previous study showed that the incorporation of GO with a metal oxide could enhance the photocatalytic activity.³³ Apparently, photocatalysis enhancement through GO is because a conjugate structure provides a pathway for the transport of charge carriers.

One specific branch of GR research dealt with GO. This could be considered as a precursor of semiconductor/GO synthesis by either chemical or thermal processes. Song *et al.*²⁹ synthesized an Ag/Ag₂CO₃/rGO composite that exhibited enhanced

photocatalytic performance for the photocatalytic oxidation of organic pollutants. Zhang *et al.*²⁸ prepared TiO₂-graphene composites for photochemical processes to ultimately degrade organic compounds into CO₂ and H₂O at ambient conditions. Yang *et al.*³⁴ reported that Ag₃PO₄/GR was applied to the suspended photocatalytic degradation of organic dyes. Bhirud *et al.*³¹ obtained a ZnO-graphene composite through a hydrothermal treatment using Zn powder as the reducing agent and precursor. Recently, BiOI/graphene,³⁵ BiOBr/graphene,³⁶ and BiOBr_xI_{1-x}/graphene³⁷ composites have been synthesized to improve the photocatalytic activity of materials. Functionalizing GO nanosheets with a series of BiO_xI_y should not only combine the advantages of both BiO_xI_y and GO nanosheets but also result in new properties. However, no work related to a series of GO-based BiO_xI_y photocatalysts has been reported.

As shown in Table 1, BiO_xI_y/GO (or rGO, GR) composites have obtained remarkable interest in recent years because of their suitable band gaps, stability, and relatively superior photocatalytic activities. It is found that the BiO_xI_y/GO (or rGO, GR) composite shows higher photocatalytic activities than BiO_xI_y and GO (or rGO, GR) for the photocatalytic degradation of rhodamine B (or methyl orange, phenol).³⁸⁻⁴²

According to our literature search, a series of BiO_xI_y/GO-assisted photocatalytic degradations of CV dyes under visible light irradiation has never been reported. This study synthesized BiOI/GO, Bi₄O₅I₂/GO, Bi₇O₉I₃/GO, and Bi₅O₇I/GO heterojunctions and compared their photocatalytic activities in degrading CV in aqueous solutions under visible light irradiation.

2. Experimental details

2.1 Materials

Graphite (Showa), isopropanol, H₂SO₄ and HCl (Merck), KMnO₄ (Shimakyu), NaNO₃, Bi(NO₃)₃·5H₂O, salicylic acid (2-hydroxybenzoic acid) and KI (Katayama), CV dye (TCI), *p*-benzoquinone (Alfa Aesar), sodium azide (Sigma), and ammonium oxalate (Osaka) were purchased and used without further purification. Reagent-grade sodium hydroxide, nitric acid,

ammonium acetate, and high pressure liquid chromatography (HPLC)-grade methanol were obtained from Merck.

2.2 Instruments and analytical methods

The amount of residual dye in each reaction cycle was determined by high performance liquid chromatography photodiode array electrospray ionization mass spectrometry (HPLC-PDA-ESI-MS). The analysis of organic intermediates was accomplished by HPLC-PDA-ESI-MS after readjustment of the chromatographic conditions in order to make the mobile phase (solvent A and B) compatible with the working conditions of the mass spectrometer. Solvent A was 25 mM aqueous ammonium acetate buffer (pH 6.9), and solvent B was methanol. LC was carried out on an AtlantisTM dC18 column (250 mm × 4.6 mm i.d., dp = 5 μm). The mobile phase flow rate was 1.0 mL min⁻¹. A linear gradient was run as follows: $t = 0, A = 95, B = 5$; $t = 20, A = 50, B = 50$; $t = 35-40, A = 10, B = 90$; $t = 45, A = 95, B = 5$. The column effluent was introduced into the ESI source of the mass spectrometer. The quadrupole mass spectrometer equipped with an ESI interface with heated nebulizer probe at 350 °C was used with an ion source temperature of 80 °C. ESI was carried out with the vaporizer at 350 °C and nitrogen as the sheath (80 psi) and auxiliary (20 psi) gas to assist with the preliminary nebulization and to initiate the ionization process. A discharge current of 5 μA was applied. The tube lens and capillary voltages were optimized for the maximum response during perfusion of the CV standard.

X-ray diffraction (XRD) patterns were recorded on a MAC Science MXP18 instrument equipped with Cu-K α radiation, operating at 40 kV and 80 mA. Field-emission transmission electron microscopy (FE-TEM) images, selected area electron diffraction patterns, high resolution transmission electron microscopy (HRTEM) images, and energy-dispersive X-ray spectroscopy (EDS) spectra were obtained using a JEOL-2010 instrument with an accelerating voltage of 200 kV. Al-K α radiation was generated at 15 kV. Field emission scanning electron microscopy electron-dispersive X-ray spectroscopy (FE-SEM-EDS) measurements were conducted using a JEOL JSM-7401F instrument at an acceleration voltage of 15 kV. High resolution X-ray photoelectron spectroscopy measurements were conducted using an ULVAC-PHI instrument. Photoluminescence (PL) measurements were conducted on a Hitachi F-7000 instrument. Ultraviolet photoelectron spectroscopic measurements were performed using an ULVAC-PHI XPS, PHI Quantera SXM. Brunauer–Emmett–Teller (BET) specific surface areas of the samples (S_{BET}) were measured with an automated system (Micrometrics Gemini) by using nitrogen gas as the adsorbate at liquid nitrogen temperature. The mineralization of BCExM was monitored by measuring the total organic carbon (TOC) content with a Dohrmann Phoenix 8000 Carbon Analyzer using a UV/persulfate oxidation method by directly injecting the aqueous solution into the instrument.

2.3 Synthesis of BiO_xI_y/GO

GO was prepared by stirring 1 g powdered flake graphite and 0.5 g NaNO₃ into 23 mL H₂SO₄ in a 0 °C ice bath. While maintaining

vigorous agitation, 3 g KMnO₄ was added to the suspension. The ice bath was then removed, and the temperature of the suspension was brought to 35 °C and maintained at that temperature overnight. Then, 3 g KMnO₄ was added to the suspension, which was allowed to stand for 3 h. After 3 h, 46 mL H₂O was slowly stirred into the paste, causing violent effervescence and a temperature increase to 95 °C. The diluted suspension, now brown in color, was maintained at this temperature for 15 min. The suspension was then further diluted to approximately 140 mL with warm water and treated with 30% (w) H₂O₂ to reduce the residual MnO₄⁻ and MnO₂ to colorless soluble Mn(SO₄)₂. Upon treatment with the peroxide, the suspension turned bright yellow. The suspension was filtered, and a yellow-brown filter cake was obtained. After washing the cake three times with a total of 140 mL warm water, the GO residue was dispersed in 100 mL of 10% HCl. Dry GO was obtained through centrifugation followed by drying in the oven at 60 °C overnight.⁴³

Five mmol Bi(NO₃)₃·5H₂O was first mixed in a 50 mL flask, followed by the addition of 5 mL 4 M ethylene glycerol and GO powder. With continuous stirring, 2 M NaOH was added dropwise to adjust the pH value; when a precipitate was formed, 2 mL KI was also added dropwise. The solution was then stirred vigorously for 30 min and transferred into a 30 mL Teflon-lined autoclave, which was heated to 100–250 °C for 12 h and then naturally cooled to room temperature. The resulting solid precipitate was collected by filtration, washed with deionized water and methanol to remove any possible ionic species in the solid precipitate, and then dried at 60 °C overnight. Depending on the molar ratio of Bi(NO₃)₃·5H₂O to KI, pH value, temperature, and time, different BiO_xI_y/GO samples could be synthesized.

2.4 Photocatalytic and active species experiments

CV irradiation experiments were conducted on a stirred aqueous solution contained in a 100 mL flask; the aqueous suspension of CV (100 mL, 10 ppm) and a catalyst powder were placed in a Pyrex flask. The pH of the suspension was adjusted by adding either NaOH or HNO₃ solution. Dark experiments were performed to examine the adsorption or desorption equilibrium. 10 mg photocatalyst was mixed with 100 mL aqueous CV solution with a known initial concentration in a 100 mL flask, and the mixture was shaken in an orbital shaker (100 rpm) at a constant temperature. The mixture was centrifuged at 3000 rpm in a centrifugation machine after batch sorption experiments so that the absorbance of CV could be determined at 580 nm through HPLC-PDA-ESI-MS. The concentrations of the solutions were determined using a linear regression equation. Prior to irradiation, the suspension was magnetically stirred in the dark for approximately 30 min to establish an adsorption or desorption equilibrium between the CV and the catalyst surface. Irradiation was conducted using 150 W Xe arc lamps; the light intensity was fixed at 31.1 W m⁻², and the reaction vessel was placed 30 cm from the light source. At given irradiation time intervals, a 5 mL aliquot was collected and centrifuged to remove the catalyst. The supernatant was measured using HPLC-PDA-ESI-MS.

A series of quenchers were introduced to scavenge the relevant active species to evaluate the effect of the active species during the photocatalytic reaction. Superoxide radicals, hydroxyl radicals, holes, and singlet oxygen ($^1\text{O}_2$) were studied by adding 1.0 mM benzoquinone (BQ, a quencher of superoxide radicals),⁴⁴ 1.0 mM isopropanol (IPA, a quencher of hydroxyl radicals),⁴⁵ 1.0 mM ammonium oxalate (AO, a quencher of holes),⁴⁶ and 1.0 mM sodium azide (SA, a quencher of singlet oxygen).⁴⁷ The method was similar to the previously reported photocatalytic activity test.^{44–47}

3. Results and discussion

3.1 Characterization of the $\text{BiO}_x\text{I}_y/\text{GO}$ heterojunction

3.1.1 Phase structure. XRD analysis was used to determine the average crystalline properties of the GO sheet. In Fig. 1, the XRD results initially proved the successful synthesis of GO sheets. The diffraction peak becomes broader in the enlarged pattern of GO at $2\theta = 12.5^\circ$, and the significant increase in d spacing is believed to be due to the following reason: oxygen functional groups intercalate in the interlayer of graphite. There is a very weak diffraction peak at $2\theta = 42.5^\circ$, which is believed to be due to the incomplete oxidation.

Fig. 1 shows the XRD patterns of the as-prepared samples; the patterns clearly show the existence of different BiO_xI_y phase composites with GO. All the as-prepared samples contained the BiOI phase (JCPDS 73-2062), $\text{Bi}_4\text{O}_5\text{I}_2$ phase,⁴⁸ $\text{Bi}_7\text{O}_9\text{I}_3$ phase,⁴⁹ $\text{Bi}_5\text{O}_7\text{I}$ phase (JCPDS 40-0548), and GO.⁵⁰ At pH = 1, the XRD patterns (Fig. 1(a)) were identical to those reported for the BiOI/GO binary phases; at pH = 4, the XRD patterns (Fig. 1(b)) were identical to those reported for the $\text{Bi}_4\text{O}_5\text{I}_2/\text{GO}$ binary phases; at pH = 7, the XRD patterns (Fig. 1(c)) were identical to those reported for the $\text{Bi}_4\text{O}_5\text{I}_2/\text{GO}$ binary phases (0.15 g) and $\text{Bi}_7\text{O}_9\text{I}_3/\text{GO}$ binary phases (0.005–0.10 g); at pH = 10, the XRD patterns (Fig. 1(d)) were identical to those reported for the $\text{Bi}_7\text{O}_9\text{I}_3/\text{GO}$ binary phases; and at pH = 13, the XRD patterns (Fig. 1(e)) were identical to those reported for the $\text{Bi}_5\text{O}_7\text{I}/\text{GO}$ binary phases. Table 2 summarizes the results of the XRD measurements.

Fig. 2 and S1–S5 of the ESI† illustrate that the as-prepared samples were composed of differently sized layers, consistent with the TEM observations. The graphene oxide nanosheets and bismuth oxyiodide are clearly observed. The graphene oxide sheets are not very flat but display intrinsic microscopic wrinkles, and bismuth oxyiodide is dispersed on the graphene oxide nanosheets. In addition, the EDS spectrum shows that the sample contained the elements of Bi, I, O, and C. In Fig. 2(a) and (b), the HRTEM image shows that two sets of different lattice images were found with a d -spacing of 0.282 nm, corresponding to the (110) plane of BiOI, which is in satisfactory agreement with the XRD results (Fig. 1(a)). In Fig. 2(c) and (d), the HRTEM image shows that two sets of different lattice images were found with a d -spacing of 0.286 nm, corresponding to the (402) plane of $\text{Bi}_4\text{O}_5\text{I}_2$, which is in satisfactory agreement with the XRD results (Fig. 1(b)). In Fig. 2(e) and (f), the HRTEM image shows that two sets of different lattice images were found with a d -spacing of 0.317 nm, corresponding to the (110) plane of $\text{Bi}_7\text{O}_9\text{I}_3$, which is in satisfactory agreement with the XRD results

(Fig. 1(c)). In Fig. 2(g) and (h), the HRTEM image shows that three sets of different lattice images were found with a d -spacing of 0.313 nm, corresponding to the (110) plane of $\text{Bi}_7\text{O}_9\text{I}_3$, which

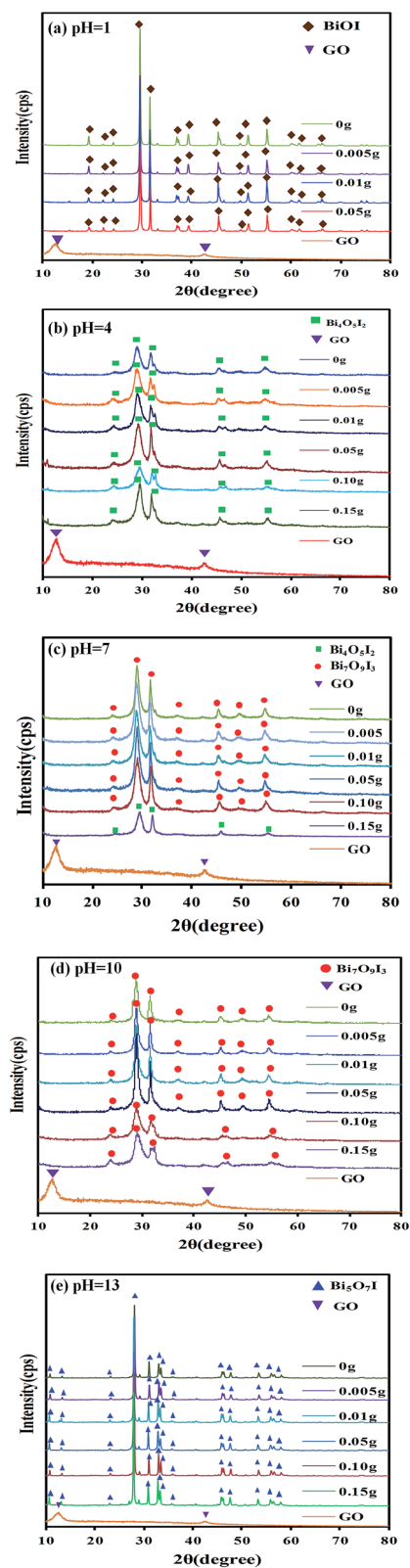


Fig. 1 XRD patterns of the as-prepared $\text{BiO}_x\text{I}_y/\text{GO}$ samples at different pH values.

Table 2 Crystalline phase changes of BiO_xI_y/GO prepared under different reaction conditions (◆ BiOI; ■ Bi₄O₅I₂; ● Bi₇O₉I₃; ▲ Bi₅O₇I; ▼ GO)

BiO _x I _y /GO	pH				
	1	4	7	10	13
Graphene oxide weight (g)					
0	◆	■	●	●	▲
0.005	◆▼	■▼	●▼	●▼	▲▼
0.01	◆▼	■▼	●▼	●▼	▲▼
0.05	◆▼	■▼	●▼	●▼	▲▼
0.10	—	■▼	●▼	●▼	▲▼
0.15	—	■▼	■▼	●▼	▲▼

is in satisfactory agreement with the XRD results (Fig. 1(d)). In Fig. 2(i) and (j), the HRTEM image shows that two sets of different lattice images were found with a *d*-spacing of 0.318 nm, corresponding to the (312) plane of Bi₅O₇I, which is in satisfactory agreement with the XRD results (Fig. 1(e)). The results suggest that the series of BiO_xI_y/GO phases were produced in the composites, which are favorable for the separation of photoinduced carriers, yielding high photocatalytic activities.

The results illustrate that at different pH values, a series of changes occurred in the products. The proposed processes for the formation of the BiO_xI_y/GO composites are described in eqn (1)–(7). The results demonstrate that a series of changes in the compounds occurred at different hydrothermal conditions, expressed as BiOI → Bi₄O₅I₂ → Bi₇O₉I₃ → Bi₅O₇I → α-Bi₂O₃. By controlling the pH of the hydrothermal reaction, different compositions of bismuth oxyiodides were obtained.

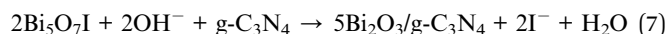
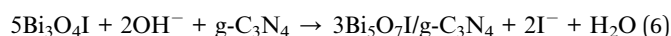
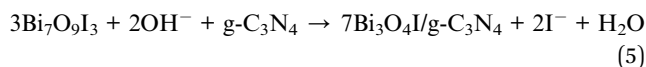
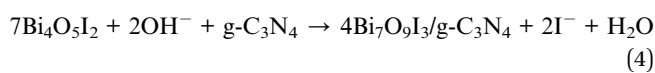


Fig. 3 shows the Fourier transform infrared (FT-IR) spectra of the Bi₇O₉I₃/GO composite produced at different weight percentages, where a strong absorption was located mainly in the range of 400–700 cm⁻¹, as a result of the stretching vibrations of Bi–O, Bi–O–I, and Bi–O–Bi in bismuth oxyiodides.⁷ The FT-IR spectrum of GO shows a strong absorption band at 3429

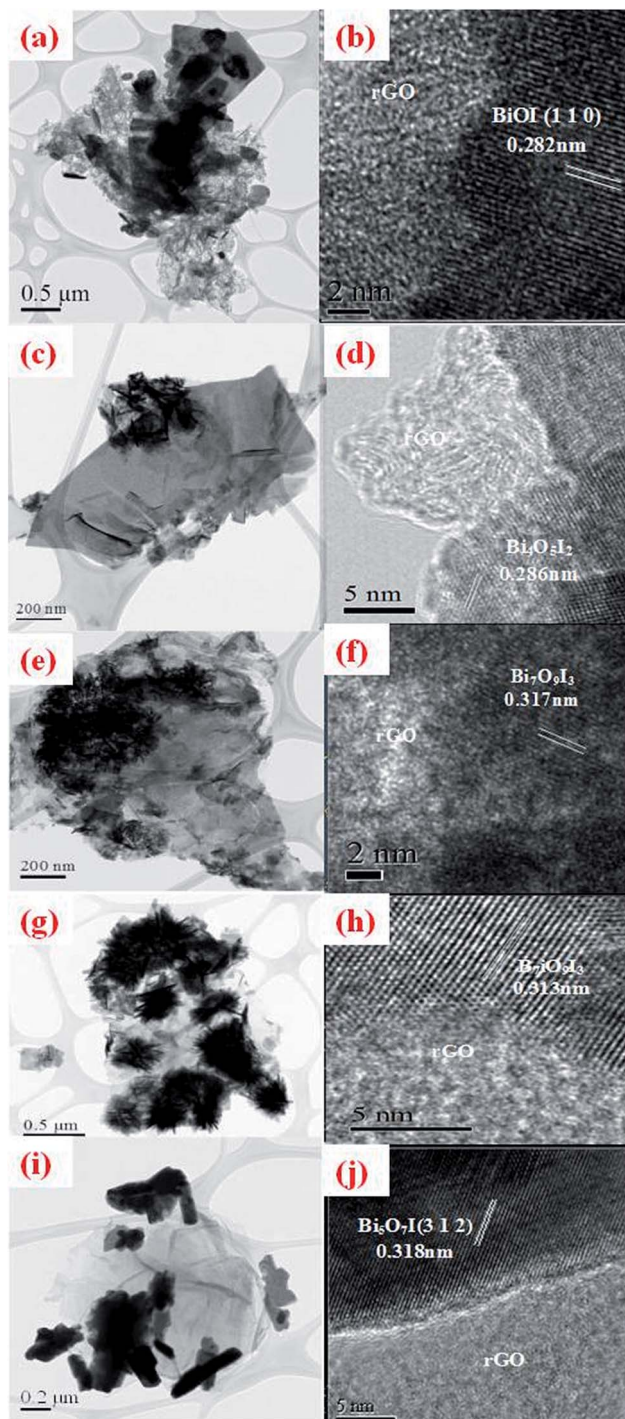


Fig. 2 FE-TEM of the as-prepared (a) and (b) BiOI/GO, (c) and (d) Bi₄O₅I₂/GO, (e) and (f) Bi₇O₉I₃/GO, (g) and (h) Bi₇O₉I₃/GO, and (i) and (j) Bi₅O₇I/GO.

cm⁻¹ because of the O–H stretching vibration. The spectrum also exhibits bands at approximately 1726 cm⁻¹ because of the C=O stretching of COOH groups situated at the edges of the GO sheets, and the O–H bending vibration, epoxide groups, and skeletal ring vibrations are observed at approximately 1631 cm⁻¹.⁵¹ The absorption at 1396 and 1000 cm⁻¹ may be attributed to tertiary C–OH and the stretching of C–O–C groups. After

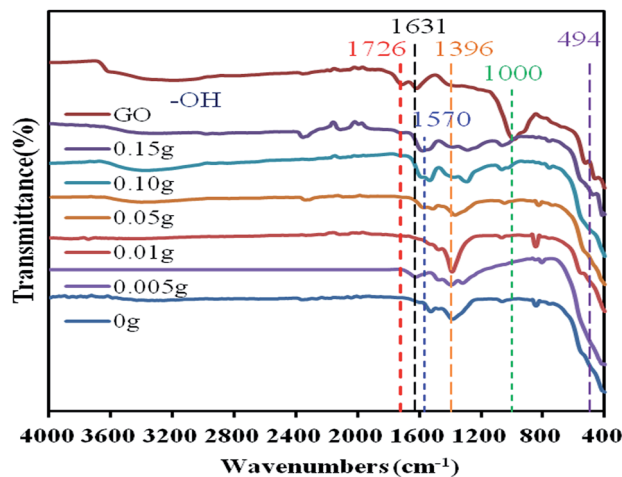


Fig. 3 FT-IR of the as-prepared $\text{Bi}_7\text{O}_9\text{I}_3/\text{GO}$ samples at $\text{pH} = 7$.

the composition process, the intensities of the absorption bands because of the O–H stretching vibration (3429 cm^{-1}) and C=O stretching vibration (1726 cm^{-1}) decreased substantially, and the band at 1631 cm^{-1} was absent.⁵² Instead, a new absorption band appeared at 1570 cm^{-1} , which was attributed to the skeletal vibration of the graphene sheets.⁵³ This result agrees with that of the XRD and TEM experiments.

3.1.2 Morphological structure and composition. A series of $\text{BiO}_x\text{I}_y/\text{GO}$ composites were synthesized through hydrothermal methods at different pH values. The surface morphologies of the as-prepared samples (Fig. S1–S5(f) of the ESI[†]) were measured using FE-SEM-EDS. The FE-SEM images show that the morphologies of the samples acquired at different pH values turned from flower-like to nanoparticles and small flower-like, and then became irregular square thin plates. The SEM-EDS and TEM-EDS results demonstrate that the main elements within these samples were bismuth, oxygen, iodine, and carbon (Fig. S1–S5(e) of the ESI[†]). From the aforementioned results, it is shown that a series of $\text{BiO}_x\text{I}_y/\text{g}-\text{C}_3\text{N}_4$ composites can be selectively synthesized through the controlled hydrothermal method.

3.1.3 X-ray photoelectron spectroscopic analysis. Fig. 4 presents the Bi 4f, I 3d, O 1s, and C 1s XPS spectra of the $\text{Bi}_7\text{O}_9\text{I}_3/\text{GO}$ composites. The observation of the transition peaks involving Bi 4f, I 3d, O 1s, and C 1s orbitals identified that the catalysts were composed of Bi, I, O, and C. The characteristic binding energy value of 158.8 eV for Bi $4f_{7/2}$ (Fig. 4(a)) shows a trivalent oxidation state for bismuth. An additional spin–orbit doublet with a binding energy of 156.6 eV for Bi $4f_{7/2}$ was also revealed in all the samples, suggesting that certain parts of bismuth existed in the $(+3-x)$ valence state. This showed that the trivalent bismuth was partially reduced to the lower valence state through the hydrothermal method. A similar chemical shift of approximately 1.9 eV for Bi $4f_{7/2}$ was published by Chen *et al.*^{7,54} They found that the $\text{Bi}^{(+3-x)}$ formal oxidation state could most probably be ascribed to the substoichiometric forms of Bi within the Bi_2O_2 layer, and the formation of the low oxidation state resulted in oxygen vacancies in the crystal lattice. However, this study assumed that the $\text{Bi}^{(+3-x)}$ formal oxidation state could most likely be ascribed to the substoichiometric forms of Bi at

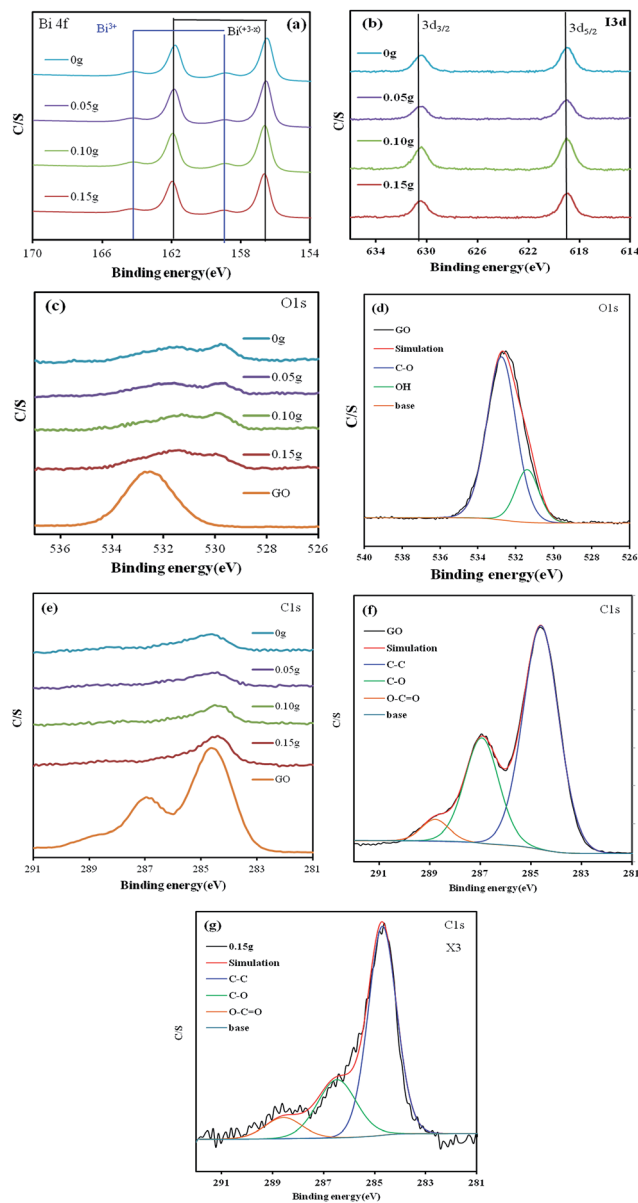


Fig. 4 XPS spectra of $\text{Bi}_7\text{O}_9\text{I}_3/\text{GO}$ ($\text{pH} = 7$) for (a) Bi 4f, (b) I 3d, (c) O 1s, (d) GO O 1s, (e) C 1s, (f) GO C 1s, and (g) 0.05 g GO C 1s.

the outer sites of the particles, and the formation of the low oxidation state resulted in oxygen vacancies in the crystal surface, revealing that the main chemical states of the bismuth element in the samples were not trivalent.

From Fig. 4(b), the binding energies of 630.7 eV and 619.1 eV were attributed to I $3d_{3/2}$ and $3d_{5/2}$, respectively, which could point to I in the monovalent oxidation state. Fig. 4(c) shows the high-resolution XPS spectra for the O 1s region of the $\text{Bi}_7\text{O}_9\text{I}_3/\text{GO}$ composites, which could be resolved into two peaks; the main peak at 529.7 eV was attributed to the Bi–O bonds in the $(\text{Bi}_2\text{O}_2)^{2+}$ slabs of the BiOX layered structure, whereas the peak at 531.3 eV was assigned to the hydroxyl groups on the surface.⁵⁵ The asymmetric O 1s peak shown in Fig. 4(d) can be split by using the XPS peak-fitting program for pure GO. The peak at 531.2 eV was assigned to the external –OH group or the water

molecule adsorbed on the surface, and the other O 1s peak appearing at 532.4 eV corresponded to the C–O bonds in the GO.⁵⁴ Fig. 4(e)–(g) show the high-resolution C 1s spectra of the Bi₇O₉I₃/GO composites and pure GO. Three carbon species were displayed mainly in the C 1s spectra of pure GO and the Bi₇O₉I₃/GO composites including unoxidized carbons (sp² carbon), C–O, and C=O. As seen in Fig. 4(f) and (g), three different chemically shifted components are visible, which could be deconvoluted into sp² carbons in aromatic rings (284.4 eV) and C atoms bonded to oxygen (C–O 286.8 eV) and carbonyls (C=O, 288.7 eV).^{56,57}

3.1.4 Optical absorption properties. As shown in Fig. 5 and Table S1 of the ESI† for the ultraviolet diffuse reflectance of various BiO_xI_y/GO composites, the absorption edge of BiO_xI_y was at about 566.2–733.8 nm, which originated from its band gap of 2.19–1.69 eV and is consistent with the reported results.⁷ The E_g value of BiO_xI_y/g-C₃N₄ was determined from a plot of $(\alpha h\nu)^{1/2}$ vs. energy ($h\nu$), which was calculated as 0.21–2.19 eV (Table S1†). The results suggest that the fabrication of the BiO_xI_y/GO composites could greatly improve the optical absorption properties and increase the utilized efficiency of solar light, which was favorable for the enhancement of the photocatalytic activity.

3.1.5 Adsorption-desorption isotherm. In Fig. 6, the BET surface area of the GO was measured to be 10.78 m² g⁻¹, far below the theoretical value of fully exfoliated pristine graphene (~2620 m² g⁻¹). The pore volume and size distribution of GO was 0.012 cm³ g⁻¹ and 4.54 nm respectively. Fig. 6 also shows the nitrogen adsorption-desorption isotherm curves of BiO_xI_y, GO, and 0.05 g BiO_xI_y/GO. The isotherms of GO were close to Type III without a hysteresis loop at a high relative pressure between 0.6 and 1.0,⁵⁸ suggesting the existence of nonporous

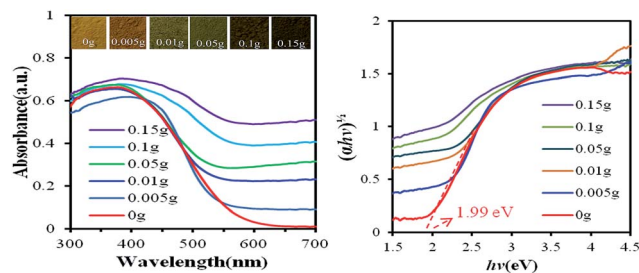


Fig. 5 DRS patterns of the as-prepared Bi₇O₉I₃/GO samples at pH = 7.

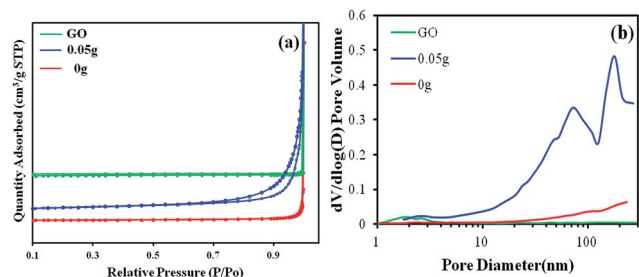


Fig. 6 (a) N₂ adsorption-desorption isotherms and (b) pore size distribution of Bi₇O₉I₃/GO at pH = 7.

GO. The isotherms of BiO_xI_y and BiO_xI_y/GO were close to Type IV with a hysteresis loop at a high relative pressure between 0.6 and 1.0.⁵⁸ The shape of the hysteresis loop was close to Type H3, suggesting the existence of slit-like pores generally formed by the aggregation of plate-like particles, which is consistent with the self-assembled nanoplate-like morphology of the samples. This result is consistent with the FE-SEM results, showing that self-assembled nanosheets or nanoplates resulted in the formation of hierarchical architectures.

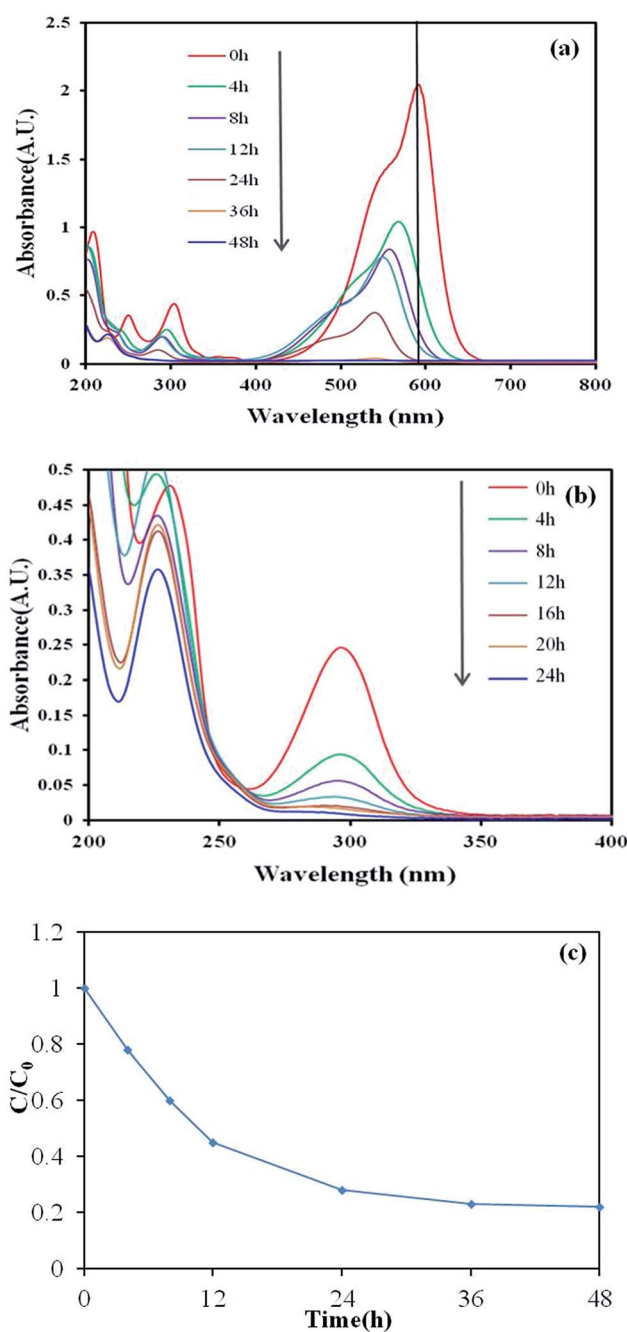


Fig. 7 Temporal UV-vis adsorption spectral changes during the photocatalytic degradation of (a) CV and (b) SA, and (c) depletion of the TOC as a function of reaction time over aqueous Bi₇O₉I₃/GO under visible light irradiation.

3.2 Photocatalytic activity

Fig. 7(a) and (b) illustrate the changes in the ultraviolet visible (UV-vis) spectra during the photodegradation process of CV and SA in aqueous Bi₇O₉I₃/GO dispersions under visible light irradiation. They were wholly degraded after visible light irradiation for 48 h (approximately 99% of CV), and after visible light irradiation for 36 h (approximately 96% of SA for 24 h). During visible light irradiation, the characteristic absorption band of the CV dye at approximately 589.0 nm decreased rapidly with a slight hypsochromic shift (545.2 nm), but no new absorption bands appeared even in the ultraviolet range ($\lambda > 200$ nm), indicating the probable formation of a series of *N*-demethylated intermediates and cleavage of the whole conjugated chromophore structure of the CV dye. Further irradiation caused the decrease of the absorption band at 545.2 nm, but no further wavelength shift was observed, inferring that the band at 545.2 nm was that of the full *N*-demethylated product of the CV dye. The complete mineralization of 1 mol CV dye molecule implies the formation of the equivalent amount (25 mol) of CO₃²⁻ at the end of the treatment. However, the depletion of the TOC (shown in Fig. 7(c)) clearly indicates that the reaction does not go to completion. In fact, after 48 min of reaction, about 74.5% of the initial organic carbon had been transformed into CO₂, which implied the existence of other organic compounds in the solution. This is supported by the HPLC-PDA-ESI-MS analysis,

which suggests the presence of residual organic products even after 48 min of reaction, confirming the noticeable degradation of the examined dye.

Tables 3 and 4 and Fig. 8 illustrate the degradation efficiency as a function of reaction time; the removal efficiency was significantly enhanced in the presence of 0.05–0.15 g Bi₇O₉I₃/GO and 0.10 g Bi₄O₅I₂/GO. To further understand the reaction kinetics of CV degradation, the apparent pseudo-first-order model,⁵⁹ $\ln(C_0/C) = kt$, was applied to the experiments. Through the first-order linear fit of the data shown in Fig. 8 and Table 3, the *k* values of 0.05 g Bi₇O₉I₃/GO and 0.10 g Bi₄O₅I₂/GO were obtained as the maximum degradation rates of 3.51×10^{-1} and $3.22 \times 10^{-1} \text{ h}^{-1}$ by using the first-order linear fit of the data, which are much higher than those of the other composites. The 0.05 g Bi₄O₅I₂/GO composite had a larger *S*_{BET} and pore volume (Table S2†). However, the results in Table S2† show that the 0.05 g Bi₇O₉I₃/GO sample—which does not show the highest *S*_{BET}—did represent the highest photocatalytic activity ($k = 3.22 \times 10^{-1} \text{ h}^{-1}$) among the samples, suggesting that the changes in the photocatalytic activity resulted from both the *S*_{BET} and the BiO_{*x*}I_{*y*}/GO composites. Table 5 shows a comparison of the rate constants of the different photocatalysts. The order of rate constants was as follows: Bi₄O₅I₂/GO > Bi₇O₉I₃/GO > Bi₄O₅I₂ > Bi₇O₉I₃ > Bi₇O₉I₃/GO > BiOI/GO > BiOI > Bi₅O₇I > GO. The photocatalytic activity of the Bi₄O₅I₂/GO (or Bi₇O₉I₃/GO)

Table 3 Pseudo-first-order rate constants for the degradation of CV with BiO_{*x*}I_{*y*}/GO heterojunctions under visible light irradiation

BiO _{<i>x</i>} I _{<i>y</i>} /GO	pH									
	1		4		7		10		13	
	<i>k</i> (h ⁻¹)	<i>R</i> ²								
0	0.027	0.940	0.198	0.949	0.190	0.954	0.191	0.983	0.004	0.973
0.005	0.020	0.976	0.252	0.967	0.255	0.973	0.183	0.973	0.012	0.985
0.01	0.051	0.942	0.256	0.931	0.277	0.982	0.192	0.970	0.005	0.910
0.05	0.050	0.940	0.218	0.953	0.351	0.953	0.191	0.955	0.065	0.914
0.10	—	—	0.322	0.924	0.286	0.976	0.272	0.904	0.014	0.944
0.15	—	—	0.080	0.913	0.311	0.913	0.319	0.911	0.034	0.865

Table 4 Pseudo-first-order rate constants for the degradation of SA with BiO_{*x*}I_{*y*}/GO heterojunctions under visible light irradiation

BiO _{<i>x</i>} I _{<i>y</i>} /GO	pH									
	1		4		7		10		13	
	<i>k</i> (h ⁻¹)	<i>R</i> ²								
0	0.005	0.615	0.250	0.947	0.239	0.982	0.314	0.939	0.010	0.816
0.005	0.007	0.550	0.145	0.910	0.203	0.818	0.119	0.986	0.003	0.952
0.01	0.006	0.912	0.181	0.931	0.167	0.989	0.170	0.777	0.001	0.631
0.05	0.008	0.618	0.135	0.807	0.209	0.912	0.134	0.984	0.005	0.574
0.10	—	—	0.130	0.868	0.201	0.916	0.136	0.927	0.002	0.486
0.15	—	—	0.019	0.765	0.128	0.869	0.110	0.839	0.003	0.617

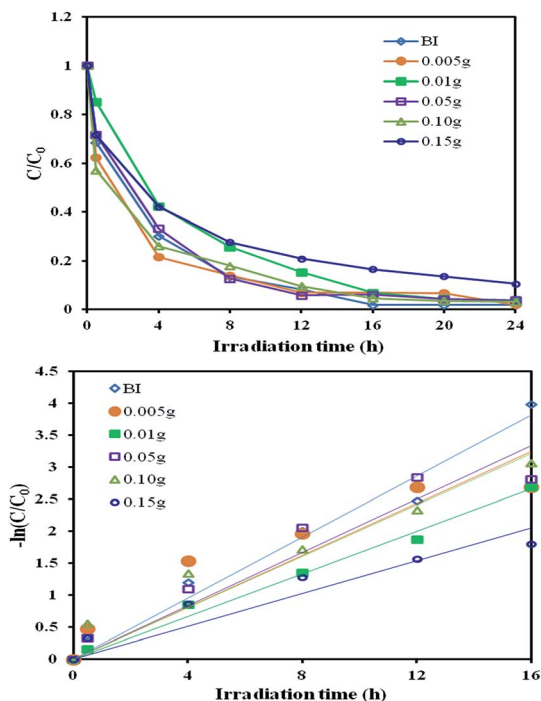


Fig. 8 Photodegradation of CV as a function of irradiation time for the different $\text{Bi}_7\text{O}_9\text{I}_3/\text{GO}$ samples (pH = 7).

heterojunctions reached a maximum rate constant of 0.351 (or 0.322) h^{-1} , which is 1.8 (or 1.7) times higher than that of $\text{Bi}_4\text{O}_5\text{I}_2$ (or $\text{Bi}_7\text{O}_9\text{I}_3$), 6–7 times higher than that of BiOI/GO , and 119–130 times higher than that of BiOI . Thus, the $\text{BiO}_x\text{I}_y/\text{GO}$ composites may also play a role in enhancing the photocatalytic activity.

However, the photocatalytic activity over the $\text{BiO}_x\text{I}_y/\text{GO}$ nanocomposites decreased when the GO content exceeded approximately 0.15 g. This decrease may be attributed to the joint effect between the excellent charge transfer capability of GO and its detrimental effect on visible light absorption. The durability of the 0.05 g $\text{Bi}_7\text{O}_9\text{I}_3/\text{GO}$ composite was evaluated by recycling the used catalyst. After each cycle, the catalyst was collected by centrifugation. No apparent decline was observed in the photocatalytic activity when CV was removed in the 3rd cycle; even during the fifth run, the decline in the photocatalytic

Table 5 Comparison of the rate constants of the different photocatalysts

Photocatalyst	Rate constant, k (h^{-1})
GO	0
BiOI	0.027
$\text{Bi}_4\text{O}_5\text{I}_2$	0.198
$\text{Bi}_7\text{O}_9\text{I}_3$	0.191
$\text{Bi}_5\text{O}_7\text{I}$	0.004
BiOI/GO	0.051
$\text{Bi}_4\text{O}_5\text{I}_2/\text{GO}$	0.322
$\text{Bi}_7\text{O}_9\text{I}_3/\text{GO}$	0.351
$\text{Bi}_5\text{O}_7\text{I}/\text{GO}$	0.065

activity was 5% (Fig. 9(a)). The used 0.05 g $\text{Bi}_7\text{O}_9\text{I}_3/\text{GO}$ composite was also examined by XRD and no detectable difference was observed between the as-prepared and the used samples (Fig. 9(b)); hence, the 0.05 g $\text{Bi}_7\text{O}_9\text{I}_3/\text{GO}$ composite had excellent photostability.

Photocatalysts are excited to generate electron-hole pairs directly after the illumination in the photocatalytic process. Photocatalytic efficiency depends mainly on the recombination rate or the lifetime of the photogenerated electron-hole pairs. The faster the recombination occurs, the shorter the chemical reaction time is. Therefore, PL spectroscopy was utilized for investigating the recombination rate of the photogenerated electron-hole pairs.⁶⁰ To investigate the separation capacity of the photogenerated carriers in the heterostructures, the PL spectra of 0.005–0.15 g $\text{Bi}_7\text{O}_9\text{I}_3/\text{GO}$ and $\text{Bi}_7\text{O}_9\text{I}_3$ were measured; the results are shown in Fig. 10. A strong emission peak at approximately 530 nm appeared for the as-prepared samples, which could have originated from the direct electron-hole recombination of band transitions. However, the characteristic emission peak within 530 nm for the 0.005–0.15 g $\text{Bi}_7\text{O}_9\text{I}_3/\text{GO}$ photocatalysts is low intensity indicated that the recombination of photogenerated charge carriers was greatly inhibited. The efficient separation of charge could increase the lifetime of the charge carriers and enhance the efficiency of interfacial charge transfer to the adsorbed substrates, thus improving the photocatalytic activity.⁵⁵ The lowest relative PL intensity of the 0.15 g

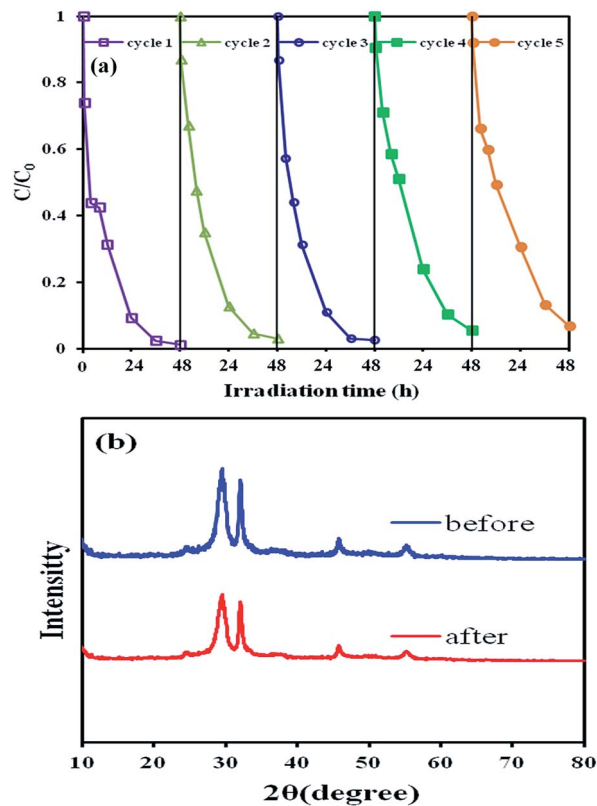


Fig. 9 (a) Cycling runs in the photocatalytic degradation of CV in the presence of $\text{Bi}_7\text{O}_9\text{I}_3/\text{GO}$ (pH = 7, 0.15 g GO); (b) XRD of the powder sample before and after the degradation reaction.

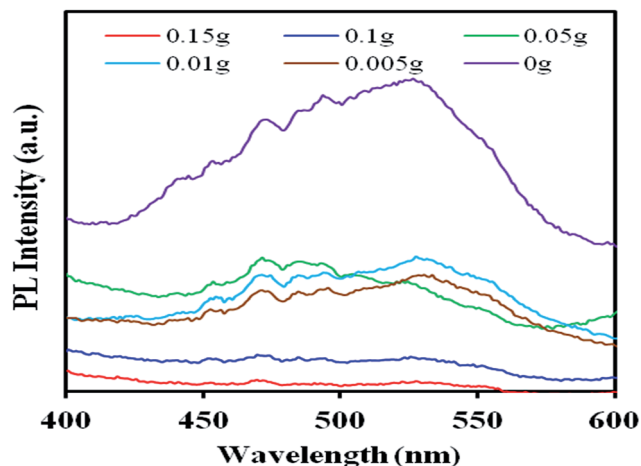


Fig. 10 PL spectrum of the $\text{Bi}_7\text{O}_9\text{I}_3/\text{GO}$ samples at $\text{pH} = 7$.

$\text{Bi}_7\text{O}_9\text{I}_3/\text{GO}$ composite, as shown in Fig. 10, suggests that it possessed a lower recombination rate of electron-hole pairs, resulting in the lower photocatalytic activity, as shown in Fig. 8. The PL results confirm the importance of the composites in hindering the recombination of electrons and holes and explain the reason for the increasing photocatalytic performance of the $\text{BiO}_x\text{I}_y/\text{GO}$ composites.

Presumably, the enhanced photocatalytic activities of $\text{BiO}_x\text{I}_y/\text{GO}$ composites could be ascribed to a synergistic effect including a high BET surface area, the formation of the composites (or heterojunction), a layered structure, and the low energy band structure. In the absence of photocatalysts, CV could not be degraded under visible light irradiation; the superior photocatalytic ability of $\text{BiO}_x\text{I}_y/\text{GO}$ may be ascribed to its efficient utilization of visible light and the high separation efficiency of the electron-hole pairs within its composites.

3.3 Active species

In general, three proposed possible reaction mechanisms are involved in the photodegradation of organisms by a semiconductor: (i) photocatalysis, (ii) photolysis, and (iii) dye photosensitization.⁶² In the photolysis process, a photoinduced electron on the induced organism directly reacts with O_2 to produce a single oxygen atom that acts as an oxidant for the pure organism photolysis.⁶³ In the present experiments, CV degradation caused by photolysis under visible light was not observable in a blank experiment; CV is a structure-stable dye, and decomposition by the photolysis mechanism was negligible.

Various primary active species, such as hydroxyl radicals, holes, superoxide radicals, hydrogen radicals (H^\cdot), and singlet oxygen, can be generated during photocatalytic decomposition processes in UV-vis/semiconductor systems.⁶³ Dimitrijevic *et al.*⁶⁴ proposed that water, which dissociated both on the surface of TiO_2 and in subsequent molecular layers, had a three-fold role as (i) a stabilizer of charges, preventing electron-hole recombination; (ii) an electron acceptor, forming H atoms in a reaction of photogenerated electrons with protons on the

surface, $-\text{OH}_2^+$; and (iii) an electron donor, resulting in the reaction of water with photogenerated holes to give $\cdot\text{OH}$ radicals.

Theoretically, GR nanosheets with 100% sp^2 -hybridized carbon atoms have a high electrical conductivity ($250\,000\text{ cm}^2\text{ V}^{-1}\text{ s}^{-1}$) for storing and shuttling electrons, and a high surface area ($2630\text{ m}^2\text{ g}^{-1}$). When GR is combined with other materials, electrons would flow from one material to the other (from a higher to a lower Fermi level) to align the Fermi energy levels at the interface of two materials.⁶⁵

Wang *et al.*⁶⁶ revealed that $\text{O}_2^{\cdot-}$ and $\cdot\text{OH}$ were the main reactive species for the degradation of rhodamine B with BiVO_4/RGO . Bai *et al.*⁶⁷ reported that active species trapping measurements, superoxide radicals ($\text{O}_2^{\cdot-}$) and hydroxy radicals played a crucial role during the catalytic process in the methylene blue degradation process using $\text{ZnWO}_4/\text{graphene}$ hybrids.⁶⁷ Shenawi-Khalil *et al.*⁶⁸ reported that $\cdot\text{OH}$ radicals were generated through the multistep reduction of $\text{O}_2^{\cdot-}$. The generation of $\text{O}_2^{\cdot-}$ could not only inhibit the recombination of photoinduced charge carriers but also benefit the dechlorination of chlorinated phenol derivatives. The hydroxyl radical HO^\cdot might only be formed through an $\text{e}^- \rightarrow \text{O}_2^{\cdot-} \rightarrow \text{H}_2\text{O}_2 \rightarrow \cdot\text{OH}$ route. However, the $\cdot\text{OH}$ radical was formed through the multistep reduction of $\text{O}_2^{\cdot-}$ in the system.⁶¹ Zhu *et al.*⁶⁹ reported that the $g\text{-C}_3\text{N}_4/\text{BiOBr}$ -mediated photodegradation of methylene blue molecules was attributed mainly to the oxidation action of the generated $\text{O}_2^{\cdot-}$ radicals and partly to the action of h^+ through the direct hole oxidation process. According to a previous study,⁶⁷ a photocatalytic process was governed mainly by $\text{O}_2^{\cdot-}$ rather than by $\cdot\text{OH}$, e^- , or h^+ . In a previous study,⁷ the CV photodegradation by $\text{BiO}_m\text{X}_n/\text{BiO}_p\text{Y}_q$ ($\text{X}, \text{Y} = \text{Cl}, \text{Br}, \text{I}$) under visible light was dominated by oxidation, with $\text{O}_2^{\cdot-}$ being the main active species and $\cdot\text{OH}$ and h^+ being the minor active species. On the basis of the aforementioned references, the probability of forming $\cdot\text{OH}$ should be much lower than that for $\text{O}_2^{\cdot-}$; however, $\cdot\text{OH}$ is an extremely strong and nonselective oxidant, which leads to a partial or complete mineralization of several organic chemicals.

Fig. 11(a) and (b) show not only the six characteristic peaks (weak) of the $\text{DMPO-O}_2^{\cdot-}$ adducts but also the four characteristic peaks (weak) of the $\text{DMPO}\cdot\text{OH}$ adducts (1 : 2 : 2 : 1 quartet pattern) under visible light irradiating the 0.05 g $\text{Bi}_7\text{O}_9\text{I}_3/\text{GO}$ composite dispersion. Fig. 11(a) and (b) indicate that no electron paramagnetic resonance (EPR) signal was observed when the reaction was performed in the dark, whereas the signals with intensities corresponding to the characteristic peaks of $\text{DMPO}\cdot\text{OH}$ and $\text{DMPO-O}_2^{\cdot-}$ adducts²² were observed during the reaction process under visible light irradiation, suggesting that $\text{O}_2^{\cdot-}$ and hydroxyl radicals ($\cdot\text{OH}$) as active species were formed in the presence of 0.05 g $\text{Bi}_7\text{O}_9\text{I}_3/\text{GO}$ composites and oxygen under visible light irradiation.

To re-evaluate the effect of the active species during the photocatalytic reaction, a series of quenchers were introduced to scavenge the relevant active species. As shown in Fig. 11(c), the photocatalytic degradation of CV was not affected by the addition of IPA, whereas the degradation efficiency of BQ, IPA, and AO quenching evidently decreased when compared with

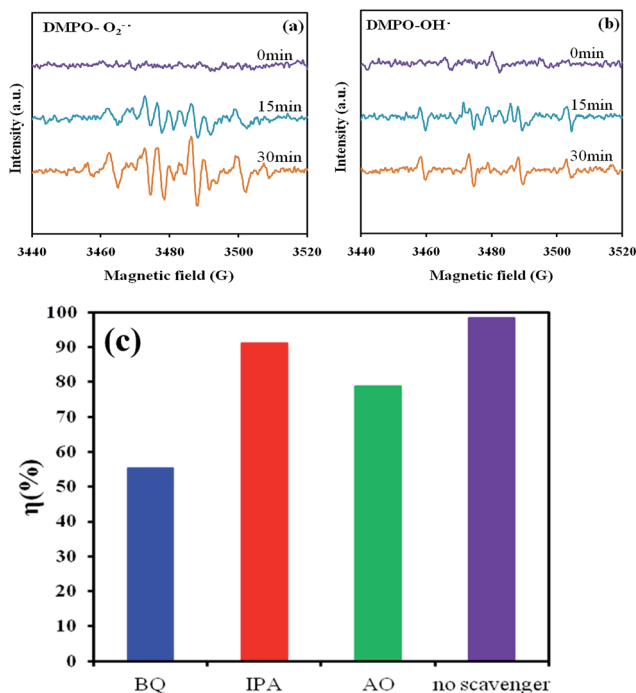


Fig. 11 (a) EPR spectra of the methanol dispersion for $\text{DMPO-O}_2^{\bullet-}$; (b) EPR spectra of the aqueous solution dispersion of DMPO-OH^{\bullet} ; (c) trapping experiments of the active species during the photocatalytic reaction involving $\text{Bi}_7\text{O}_9\text{I}_3/\text{GO}$ (pH = 7, 0.05 g GO).

that of no quenching. $\text{O}_2^{\bullet-}$ was a major active species and h^+ and hydroxyl radicals were minor active species in the process of photocatalytic degradation of CV. Therefore, the quenching effects of different scavengers and EPR indicated that the reactive superoxide radical played a major role, and holes and hydroxyl radicals played a minor role in CV photocatalytic degradation.

On the basis of the aforementioned experimental results, a detailed pathway of decomposition is illustrated in Fig. 12. Once the electron reached the conduction band of BiO_xI_y , it induced the formation of active oxygen species, which caused the decomposition of the CV dye. Except for the photodegradation of CV through the route of $\text{BiO}_x\text{I}_y/\text{GO}$ -mediated and

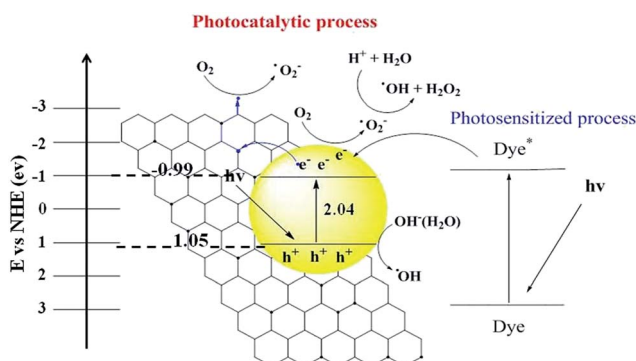
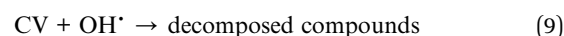
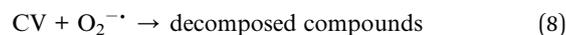


Fig. 12 Band structure diagram of $\text{Bi}_7\text{O}_9\text{I}_3/\text{GO}$ and possible charge separation processes.

photosensitized processes, another type of photocatalytic route accounted for the enhanced photocatalytic activity. Both photosensitized and photocatalytic processes proceeded concurrently (Fig. 12). However, under the photosensitized and photocatalytic reaction conditions, $\text{O}_2^{\bullet-}$ radicals were formed by the reaction of photogenerated and photosensitized electrons with oxygen gas on the photocatalyst surface; hydroxyl radicals were also produced by the reaction of $\text{O}_2^{\bullet-}$ radicals with H^+ ions and h^+ holes with OH^- ions (or H_2O). The hydroxyl radicals were produced subsequently.⁷⁰ This cycle continuously occurred when the system was exposed to visible light irradiation;⁸ after several cycles of photooxidation, the decomposition of CV by the generated oxidant species can be expressed by eqn (8) and (9).



Hydroxylated compounds were identified for the photocatalytic degradation of CV under visible light-induced semiconductor systems.⁷ Under UV light irradiation, *N*-dealkylation processes were preceded by the formation of a nitrogen-centered radical, and the destruction of the dye chromophore structure was preceded by the generation of a carbon-centered radical in the photocatalytic degradation of the CV dye.^{8,70,71} All the intermediates identified in these two researched topics had the same results under UV or visible light irradiation. Undoubtedly, the major oxidant was OH^{\bullet} radicals, not $\text{O}_2^{\bullet-}$ radicals. The reaction pathways of $\text{BiO}_x\text{I}_y/\text{GO}$ -mediated photocatalytic processes proposed in this study should offer some guidance for applications in the decomposition of dyes.

3.4 Separation and identification of the intermediates

The reaction intermediates were examined by HPLC using a photodiode array detector and ESI mass spectrometry. The results of the HPLC chromatograms, UV-visible spectra, and HPLC-ESI mass spectra are summarized in Table S3 of the ESI.† The nineteen intermediates were identified and all had retention times under 45 min. The chromatograms at pH 5 are identified as peaks A–J, a–f, and α – γ in Fig. 13(a) and (c) and were recorded at 580, 350, and 300 nm, respectively. Except for the initial CV dye (peak A), the rest of the peaks appear at the end of the 24 h of reaction, indicating the formation and transformation of intermediates.

The absorption spectra of each intermediate in the absorption spectral region are measured corresponding to the peaks. The data show that the absorption spectral bands shift hypsochromically from 588.2 nm to 543.4 nm (A–J), 376.4 to 337.5 nm (a–f), and 309.7 to 278.1 nm (α – γ) in Table S3 of the ESI.† As can be seen, the 19 compounds can be distributed into three different aromatic groups: (i) intermediates of the *N*-demethylation of *N,N,N',N',N'',N''*-hexamethylpararosaniline (CV; A), (ii) intermediates of the *N*-demethylation of 4-(*N,N*-dimethylamino)-4'-(*N',N'*-dimethylamino)benzophenone (a), and (iii) intermediates of the *N*-demethylation of 4-(*N,N*-dimethylamino)

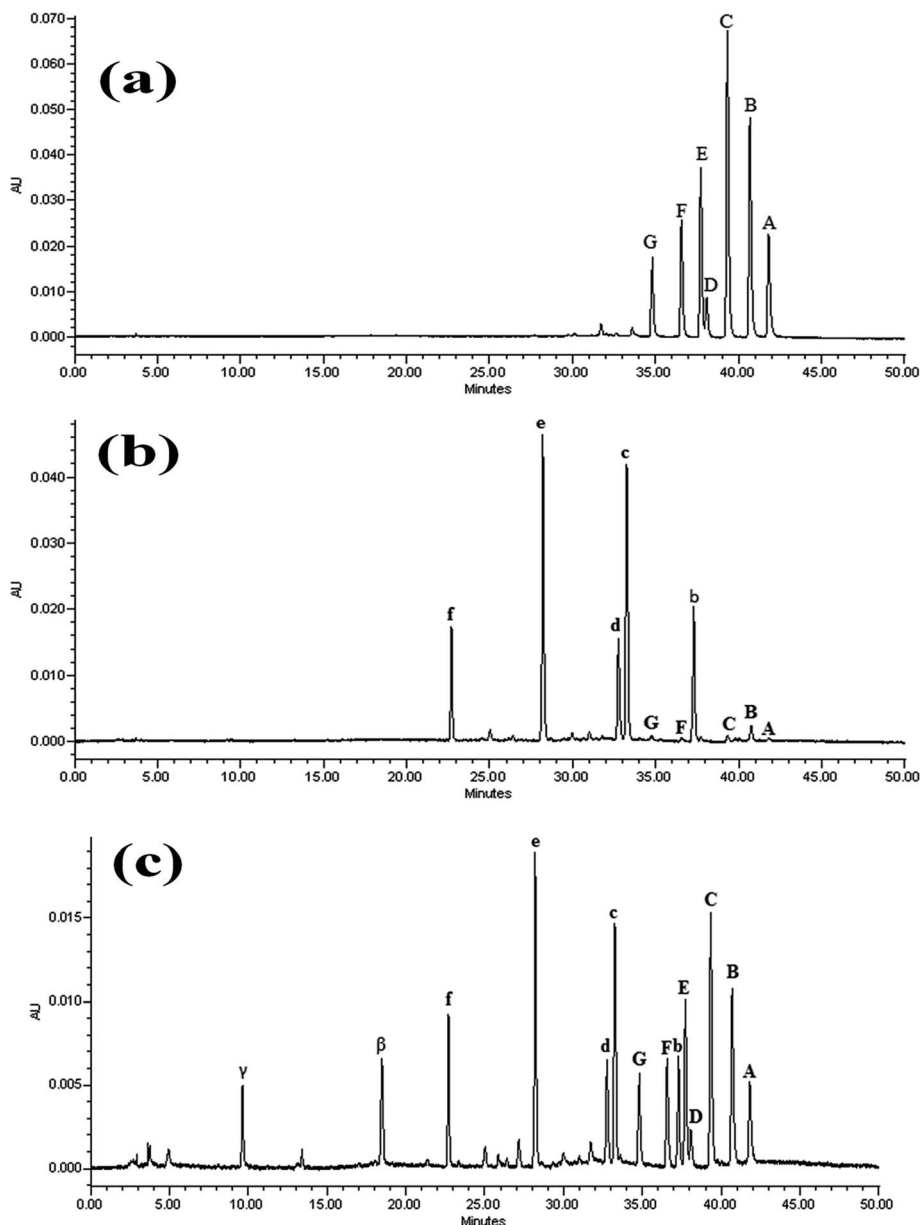


Fig. 13 HPLC chromatogram of the intermediates with 24 h of photocatalytic reaction, recorded at (a) 580 nm, (b) 350 nm, and (c) 300 nm.

phenol (α), respectively. This hypsochromic shift of the absorption band was possible due to the formation of a series of *N*-demethylated intermediates in a stepwise manner. For example, the λ_{\max} of **A**, **B**, **C**, **D**, **E**, **F**, **G**, **H**, **I**, and **J** are 588.2, 581.1, 573.4, 579.5, 566.7, 570.1, 561.8, 566.2, 554.1 and 543.4 nm, respectively; the λ_{\max} of **a**, **b**, **c**, **d**, **e**, and **f** are 376.4, 366.4, 364.4, 358.8, 357.3, and 337.5 nm, respectively; and the λ_{\max} of α , β , and γ are 309.7, 283.6, and 278.1 nm, respectively. Similar phenomena were observed during the photocatalytic degradation of CV.^{6,12} The wavelength shift depicted in Table S3 of the ESI[†] is caused by the *N*-demethylation of CV because of the attack by one of the $\cdot\text{OH}$ radicals on the *N,N*-dimethyl group. Correspondingly, the *N*-demethylated intermediates of the photocatalytic reactions were further identified using the HPLC-ESI mass spectrometric method due to a similar situation in the

intermediates category. Therefore, we used the higher removal rate of the $\text{Bi}_7\text{O}_9\text{I}_3/\text{GO}$ composite to identify the intermediates by HPLC-ESI mass spectrometry.

The *N*-demethylated intermediates were further identified using the HPLC-ESI mass spectrometric method. The molecular ion peaks appeared in the acid forms of the intermediates. As shown in Table S3,[†] the mass spectral analysis confirmed the components **A** ($m/z = 372.18$), **B** ($m/z = 358.14$), **C** ($m/z = 344.10$), **D** ($m/z = 344.09$), **E** ($m/z = 330.10$), **F** ($m/z = 330.36$), **G** ($m/z = 316.11$), **H** ($m/z = 316.11$), **I** ($m/z = 302.06$), **J** ($m/z = 288.07$), **a** ($m/z = 269.05$), **b** ($m/z = 255.06$), **c** ($m/z = 240.92$), **d** ($m/z = 240.98$), **e** ($m/z = 226.84$), **f** ($m/z = 213.06$), α ($m/z = 138.16$), β ($m/z = 124.03$), and γ ($m/z = 110.14$). These species correspond to three pairs of isomeric molecules with two to four less methyl groups than CV. For example, **B** is formed by the

removal of a methyl group from two different sides of the CV molecule, while the other corresponding isomer in this pair, **D**, is produced by the removal of two methyl groups from the same side of the CV structure. In the second pair of isomers, **E** is formed by the removal of three methyl groups from each side of the CV molecule, while the other isomer in this pair, **F**, is produced by the removal of two methyl groups from one side of the CV structure while one more methyl group was removed from the other side of the CV structure. In the third pair of isomers, **H** is formed by the removal of two methyl groups from two different sides of the CV molecule, while the other isomer in this pair, **G**, is produced by the removal of two methyl groups from the same side of the CV structure and by removal of a methyl group from the remaining two sides of the CV structure. Because the polarities of the **D**, **F** and **H** species are greater than those of the **C**, **E** and **G** intermediates, the latter were eluted after the **D**, **F** and **H** species, respectively. Since the two *N*-methyl groups are stronger auxochromic moieties than the *N,N*-dimethyl groups and the amino group, the maximal absorption of the **D**, **F** and **H** intermediates was anticipated to occur at wavelengths longer than the band position of the **C**, **E** and **G** species, respectively (Table S3 of the ESI†). On the other hand, the oxidation process is initiated by hydroxylation of the central carbon of CV. For example, the intermediates 4-(*N,N*-dimethylamino)-4'-(*N,N'*-dimethylamino)benzophenone (**a**) and 4-(*N,N*-dimethylamino)phenol (**α**) are formed by an $\cdot\text{OH}$ radical attack on the conjugated structure, yielding a carbon-centered radical, which is subsequently attacked by molecular oxygen, leading to cleavage of the CV conjugated chromophore structure. Afterwards, compounds **a** and **α** were possibly formed by a series of *N*-demethylated intermediates in a stepwise manner. This was also reported for the photocatalytic reaction of CV.^{6,11,12}

3.5 Photodegradation mechanisms of CV

Based on the HPLC-MS analyses of the various CV intermediates, the degradation pathways for CV are proposed in Fig. 14. It involves two different pathways (routes 1 and 2, respectively), corresponding to the two possible sites for the attack by $\cdot\text{OH}$ radicals on the CV molecule. As most of the $\cdot\text{OH}$ are generated directly from the photocatalytic reaction, the $\cdot\text{OH}$ species is shown as the main oxidant, though the parallel action of less oxidizing agents like $\text{HO}_2\cdot$ and H_2O_2 is not discounted. The *N*-demethylation of CV occurs mostly through attack by $\cdot\text{OH}$ species on the *N,N*-dimethyl groups of CV, as shown in Fig. S6 of the ESI† (route 1). Compound **B** is attacked by $\cdot\text{OH}$ radicals on the methyl group, and the formation of hydroxymethylated intermediates,^{70,71} which are themselves subsequently attacked by $\cdot\text{OH}$ radicals, leads ultimately to *N*-demethylation. The mono-demethylated dye, **B** intermediates, can also be attacked by $\cdot\text{OH}$ radicals on the methyl group, and then the hydroxymethylation and *N*-demethylation process described above continues until the formation of the completely *N*-demethylated dye, **F** intermediates. In addition to the *N*-demethylation degradation route, an alternative pathway was also identified. A plausible mechanism for the formation of degradation products **a-f** and **α-γ** involving reaction with $\cdot\text{OH}$ radicals formed in the

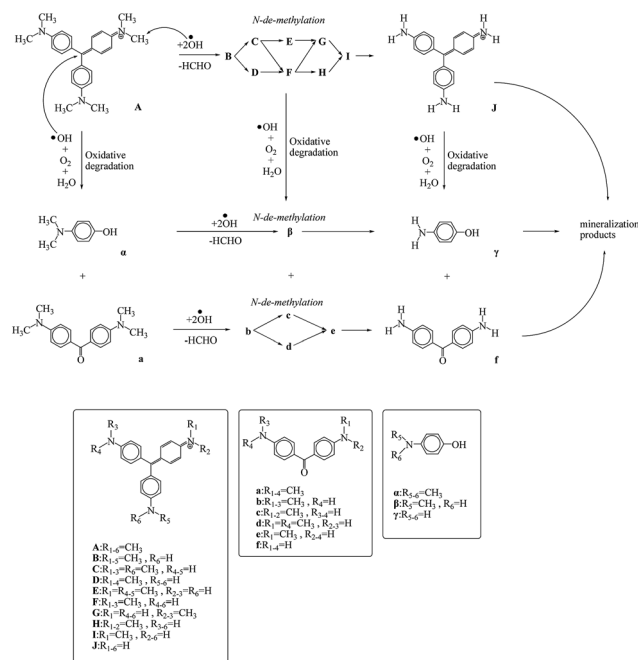


Fig. 14 Proposed degradation mechanism of CV under photocatalytic processes, followed by the identification of several intermediates by HPLC-ESI mass spectral techniques.

photocatalytic process is proposed in Fig. S7 of the ESI† (route 2). The $\cdot\text{OH}$ radical attack on the conjugated structure yields a carbon-centered radical, which is subsequently attacked by molecular oxygen to lead ultimately to the formation of 4-(*N,N*-dimethylamino)-4'-(*N,N'*-dimethylamino)benzophenone (**a**) and 4-(*N,N*-dimethylamino)phenol (**α**). It is known from previous photocatalytic studies that,^{6,11,70} after the formation of various aromatic derivatives, cleavage of the benzene or other organic rings takes place, and different aliphatic products are subsequently formed before complete mineralization. Even though further oxidation leads to the ring-opening and the formation of aliphatic oxidation products, these species will not be discussed here.

4. Conclusions

Previous studies showed that the incorporation of GO with a metal oxide could enhance photocatalytic activity. To the best of our knowledge, a series of the $\text{BiO}_x\text{I}_y/\text{GO}$ -assisted photocatalytic degradations of the CV dye under visible light irradiation has never been reported. This is the first report where four composites of BiOI/GO , $\text{Bi}_4\text{O}_5\text{I}_2/\text{GO}$, $\text{Bi}_7\text{O}_9\text{I}_3/\text{GO}$, and $\text{Bi}_5\text{O}_7\text{I}/\text{GO}$ have been synthesized through a simple hydrothermal method. The assembled $\text{BiO}_x\text{I}_y/\text{GO}$ exhibited excellent photocatalytic activity in the degradation of CV under visible light irradiation. The order of rate constants was as follows: $\text{Bi}_7\text{O}_9\text{I}_3/\text{GO} > \text{Bi}_4\text{O}_5\text{I}_2/\text{GO} > \text{Bi}_4\text{O}_5\text{I}_2 > \text{Bi}_7\text{O}_9\text{I}_3 > \text{Bi}_5\text{O}_7\text{I}/\text{GO} > \text{BiOI}/\text{GO} > \text{BiOI} > \text{Bi}_5\text{O}_7\text{I} > \text{GO}$. Thus, the $\text{BiO}_x\text{I}_y/\text{GO}$ composites played a major role in enhancing the photocatalytic activity. The quenching effects of different scavengers and EPR demonstrated that reactive $\text{O}_2^{\cdot-}$ played a major role and h^+ and $\cdot\text{OH}$ played a minor role in CV

degradation. Chiefly, composite systems exhibited adequate catalytic activity and stability, acting as authentic heterogeneous visible light-driven photocatalysts in degrading organic pollutants efficiently.

Notes and references

- 1 D. F. Duxbury, The photochemistry and photophysics of triphenylmethane dyes in solid and liquid media, *Chem. Rev.*, 1993, **93**, 381–433.
- 2 T. Inoue, K. Kikuchi, K. Hirose, M. Iiono and T. Nagano, Small molecule-based laser inactivation of inositol 1,4,5-trisphosphate receptor, *Chem. Biol.*, 2001, **8**, 9–15.
- 3 R. Bonnett and G. Martinez, Photobleaching of sensitizers used in photodynamic therapy, *Tetrahedron*, 2001, **57**, 9513–9547.
- 4 B. P. Cho, T. Yang, L. R. Blankenship, J. D. Moody, M. Churchwell, F. A. Bebland and S. J. Culp, Synthesis and Characterization of *N*-Demethylated Metabolites of Malachite Green and Leucomalachite Green, *Chem. Res. Toxicol.*, 2003, **16**, 285–294.
- 5 A. Kubacka, M. Fernández-García and G. Colón, Advanced Nanoarchitectures for Solar Photocatalytic Applications, *Chem. Rev.*, 2012, **112**, 1555–1614.
- 6 Y. R. Jiang, H. P. Lin, W. H. Chung, Y. M. Dai, W. Y. Lin and C. C. Chen, Controlled hydrothermal synthesis of BiO_xCl_y/BiO_mI_n composites exhibiting visible-light photocatalytic degradation of crystal violet, *J. Hazard. Mater.*, 2015, **283**, 787–805.
- 7 W. W. Lee, C. S. Lu, C. W. Chuang, Y. J. Chen, J. Y. Fu, C. W. Siao and C. C. Chen, Synthesis of bismuth oxyiodides and their composites: characterization, photocatalytic activity, and degradation mechanisms, *RSC Adv.*, 2015, **5**, 23450–23463.
- 8 Y. R. Jiang, S. Y. Chou, J. Lin Chang, S. T. Huang, H. P. Lin and C. C. Chen, Hydrothermal synthesis of bismuth oxybromide-bismuth oxyiodide composites with highly visible light photocatalytic performance for the degradation of CV and phenol, *RSC Adv.*, 2015, **5**, 30851–30860.
- 9 F. Chen, P. Fang, Y. Gao, Z. Liu, Y. Liu and Y. Dai, Effective removal of high-chroma crystal violet over TiO₂-based nanosheet by adsorption-photocatalytic degradation, *Chem. Eng. J.*, 2012, **204–206**, 107–113.
- 10 K. Yu, S. Yang, C. Liu, H. Chen, H. Li, C. Sun and S. A. Boyd, *Environ. Sci. Technol.*, 2012, **46**, 7318–7326.
- 11 W. L. W. Lee, J. S. Lin, J. L. Chang, J. Y. Chen, M. C. Cheng and C. C. Chen, Photodegradation of CV over nanocrystalline bismuth tungstate prepared by hydrothermal synthesis, *J. Mol. Catal. A: Chem.*, 2012, **361–362**, 80–90.
- 12 W. L. W. Lee, W. H. Chung, W. S. Huang, W. C. Lin, W. Y. Lin, Y. R. Jiang and C. C. Chen, Photocatalytic activity and mechanism of nano-cubic barium titanate prepared by a hydrothermal method, *J. Taiwan Inst. Chem. Eng.*, 2013, **44**, 660–669.
- 13 S. Ameen, M. S. Akhtar, M. Nazim and H. S. Shin, Rapid photocatalytic degradation of crystal violet dye over ZnO flower nanomaterials, *Mater. Lett.*, 2013, **96**, 228–232.
- 14 W. Wang, M. O. Tadé and Z. Shao, Research progress of perovskite materials in photocatalysis- and photovoltaics-related energy conversion and environmental treatment, *Chem. Soc. Rev.*, 2015, **44**, 5371–5408.
- 15 S. Gupta and V. Subramanian, Encapsulating Bi₂Ti₂O₇ (BTO) with Reduced Graphene Oxide (RGO): An Effective Strategy to Enhance Photocatalytic and Photoelectrocatalytic Activity of BTO, *ACS Appl. Mater. Interfaces*, 2014, **6**, 18597–18608.
- 16 H. Cheng, B. Huang and Y. Dai, Engineering BiOX (X = Cl, Br, I) nanostructures for highly efficient photocatalytic applications, *Nanoscale*, 2014, **6**, 2009–2026.
- 17 J. Li, Y. Yu and L. Zhang, Bismuth oxyhalide nanomaterials: layered structures meet photocatalysis, *Nanoscale*, 2014, **6**, 8473–8488.
- 18 J. Shang, W. Hao, X. Lv, T. Wang, X. Wang, Y. Du, S. Dou, T. Xie, D. Wang and J. Wang, Bismuth Oxybromide with Reasonable Photocatalytic Reduction Activity under Visible Light, *ACS Catal.*, 2014, **4**, 954–961.
- 19 Y. Huo, J. Zhang, M. Miao and Y. Jin, Solvothermal synthesis of flower-like BiOBr microspheres with highly visible-light photocatalytic performances, *Appl. Catal., B*, 2012, **111–112**, 334–341.
- 20 Q. C. Liu, D. K. Ma, Y. Y. Hu, Y. W. Zeng and S. M. Huang, Various Bismuth Oxyiodide Hierarchical Architectures: Alcohothermal-Controlled Synthesis, Photocatalytic Activities, and Adsorption Capabilities for Phosphate in Water, *ACS Appl. Mater. Interfaces*, 2013, **5**, 11927–11934.
- 21 H. Gnyam and Y. Sasson, Hierarchical Nanostructured 3D Flowerlike BiOCl_xBr_{1-x} Semiconductors with Exceptional Visible Light Photocatalytic Activity, *ACS Catal.*, 2013, **3**, 186–191.
- 22 X. Xiao, C. Xing, G. He, X. Zuo, J. Nan and L. Wang, Solvothermal synthesis of novel hierarchical Bi₄O₅I₂ nanoflakes with highly visible light photocatalytic performance for the degradation of 4-*tert*-butylphenol, *Appl. Catal., B*, 2014, **148–149**, 154–163.
- 23 W. L. Huang and Q. S. Zhu, DFT calculations on the electronic structures of BiOX (X = F, Cl, Br, I) photocatalysts with and without semicore Bi 5d states, *J. Comput. Chem.*, 2009, **30**, 183–190.
- 24 X. Xiao, C. Liu, R. Hu, X. Zuo, J. Nan, L. Li and L. Wang, Oxygen-rich bismuth oxyhalides: generalized one-pot synthesis, band structures and visible-light photocatalytic properties, *J. Mater. Chem.*, 2012, **22**, 22840–22843.
- 25 X. Xiao, R. Hu, C. Liu, C. Xing, C. Qian, X. Zuo, J. Nan and L. Wang, Facile large-scale synthesis of β-Bi₂O₃ nanospheres as a highly efficient photocatalyst for the degradation of acetaminophen under visible light irradiation, *Appl. Catal., B*, 2013, **140–141**, 433–443.
- 26 Q. J. Xiang, J. G. Yu and M. Jaroniec, Graphene-Based Semiconductor Photocatalysts, *Chem. Soc. Rev.*, 2012, **41**, 782–796.

- 27 N. Zhang, Y. H. Zhang and Y. J. Xu, Recent Progress on Graphene-Based Photocatalysts: Current Status and Future Perspectives, *Nanoscale*, 2012, **4**, 5792–5813.
- 28 L. Zhang, S. Diao, Y. Nie, K. Yan, N. Liu, B. Dai, Q. Xie, A. Reina, J. Kong and Z. Liu, Photocatalytic Patterning and Modification of Graphene, *J. Am. Chem. Soc.*, 2011, **133**, 2706–2713.
- 29 S. Song, B. Cheng, N. Wu, A. Meng, S. Cao and J. Yu, Structure Effect of Graphene on the Photocatalytic Performance of Plasmonic Ag/Ag₂CO₃-rGO for Photocatalytic Elimination of Pollutants, *Appl. Catal., B*, 2016, **181**, 71–78.
- 30 K. Chang, Z. Mei, T. Wang, Q. Kang, S. Ouyang and J. Ye, MoS₂/Graphene Cocatalyst for Efficient Photocatalytic H₂ Evolution under Visible Light Irradiation, *ACS Nano*, 2014, **8**, 7078–7087.
- 31 A. Bhirud, S. Sathaye, R. Waichal, C. J. Park and B. Kale, *In situ* Preparation of N-ZnO/graphene Nanocomposites: Excellent Candidate as a Photocatalyst for Enhanced Solar Hydrogen Generation and High Performance Supercapacitor Electrode, *J. Mater. Chem. A*, 2015, **3**, 17050–17063.
- 32 A. Trapalis, N. Todorova, T. Giannakopoulou, N. Boukos, T. Speliotis, D. Dimotikali and J. Yu, TiO₂/graphene composite photocatalysts for NO_x removal: a comparison of surfactant-stabilized graphene and reduced graphene oxide, *Appl. Catal., B*, 2016, **180**, 637–647.
- 33 I. V. Lightcap, T. H. Kosel and P. V. Kamat, Anchoring Semiconductor and Metal Nanoparticles on a Two-Dimensional Catalyst Mat. Storing and Shuttling Electrons with Reduced Graphene Oxide, *Nano Lett.*, 2010, **10**, 577–583.
- 34 X. Yang, H. Cui, Y. Li, J. Qin, R. Zhang and H. Tang, Fabrication of Ag₃PO₄-graphene composites with highly efficient and stable visible light photocatalytic performance, *ACS Catal.*, 2013, **3**, 363–369.
- 35 H. Liu, W. R. Cao, Y. Su, Z. Chen and Y. Wang, Bismuth oxyiodide-Graphene nanocomposites with high visible light photocatalytic activity, *J. Colloid Interface Sci.*, 2013, **398**, 161–167.
- 36 X. X. Wei, C. M. Chen, S. Q. Guo, F. Guo, X. M. Li, X. X. Wang, H. T. Cui, L. F. Zhao and W. Li, Advanced visible-light-driven photocatalyst BiOBr-TiO₂-graphene composite with graphene as a nano-filler, *J. Mater. Chem. A*, 2014, **2**, 4667–4675.
- 37 H. Liu, Y. Su, Z. Chen, Z. Jin and Y. Wang, Graphene sheets grafted three-dimensional BiOBr_{0.2}I_{0.8} microspheres with excellent photocatalytic activity under visible light, *J. Hazard. Mater.*, 2014, **266**, 75–83.
- 38 R. He, S. Cao, D. Guo, B. Cheng, S. Wageh, A. A. Al-Ghamdi and J. Yu, 3D BiOI-GO composite with enhanced photocatalytic performance for phenol degradation under visible-light, *Ceram. Int.*, 2015, **41**, 3511–3517.
- 39 H. Liu, Y. Su, Z. Chen, Z. Jin and Y. Wang, Bi₇O₉I₃/reduced graphene oxide composite as an efficient visible-light-driven photocatalyst for degradation of organic contaminants, *J. Mol. Catal. A: Chem.*, 2014, **391**, 175–182.
- 40 Z. Liu, W. Xu, J. Fang, X. Xu, S. Wu, X. Zhu and Z. Chen, Decoration of BiOI quantum size nanoparticles with reduced graphene oxide in enhanced visible-light-driven photocatalytic studies, *Appl. Surf. Sci.*, 2012, **259**, 441–447.
- 41 H. Huang, K. Liu, Y. Zhang, K. Chen, Y. Zhang and N. Tian, Tunable 3D hierarchical graphene-BiOI nanoarchitectures: their *in situ* preparation, and highly improved photocatalytic performance and photoelectrochemical properties under visible light irradiation, *RSC Adv.*, 2014, **4**, 49386–49394.
- 42 H. Liu, W. R. Cao, Y. Su, Z. Chen and Y. Wang, Bismuth oxyiodide-graphene nanocomposites with high visible light photocatalytic activity, *J. Colloid Interface Sci.*, 2013, **398**, 161–167.
- 43 W. S. Hummers and R. E. Offeman, Preparation of Graphitic Oxides, *J. Am. Chem. Soc.*, 1958, **80**, 1339.
- 44 M. C. Yin, Z. S. Li, J. H. Kou and Z. G. Zou, Mechanism investigation of visible light-induced degradation in a heterogeneous TiO₂/Eos in Y/rhodamine B system, *Environ. Sci. Technol.*, 2009, **43**, 8361–8366.
- 45 L. S. Zhang, K. H. Wong, H. Y. Yip, C. Hu, J. C. Yu, C. Y. Chan and P. K. Wong, Effective Photocatalytic Disinfection of *E. coli* K-12 Using AgBr-AgBi₂-WO₆ Nanojunction System Irradiated by Visible Light: The Role of Diffusing Hydroxyl Radicals, *Environ. Sci. Technol.*, 2010, **44**, 1392–1398.
- 46 S. G. Meng, D. Z. Li, M. Sun, W. J. Li, J. X. Wang, J. Chen, X. Z. Fu and G. C. Xiao, Sonochemical synthesis, characterization and photocatalytic properties of a novel cube-shaped CaSn(OH)₆, *Catal. Commun.*, 2011, **12**, 972–975.
- 47 G. Li, K. H. Wong, X. Zhang, C. Hu, J. C. Yu, R. C. Y. Chan and P. K. Wong, Degradation of acid orange 7 using magnetic AgBr under visible light: the roles of oxidizing species, *Chemosphere*, 2009, **76**, 1185–1191.
- 48 X. Xiao, C. Liu, R. Hu, X. Zuo, J. Nan, L. Li and L. Wang, Oxygen-rich bismuth oxyhalides: generalized one-pot synthesis, band structures and visible-light photocatalytic properties, *J. Mater. Chem.*, 2012, **22**, 22840–22843.
- 49 X. Xiao and W. D. Zhang, Hierarchical Bi₇O₉I₃ micro/nano-architecture: facile synthesis, growth mechanism, and high visible light photocatalytic performance, *RSC Adv.*, 2011, **1**, 1099–1105.
- 50 H. Liu, Y. Su, Z. Chen, Z. Jin and Y. Wang, Bi₇O₉I₃/Reduced Graphene Oxide Composite as an Efficient Visible-Light-Driven Photocatalyst for Degradation of Organic Contaminants, *J. Mol. Catal. A: Chem.*, 2014, **391**, 175–182.
- 51 C. Nethravathi and M. Rajamathi, Chemically Modified Graphene Sheets Produced by the Solvothermal Reduction of Colloidal Dispersions of Graphite Oxide, *Carbon*, 2008, **46**, 1994–1998.
- 52 P. Dong, Y. Wang, B. Cao, S. Xin, H. L. Guo, J. Zhang and F. Li, Ag₃PO₄/Reduced Graphite Oxide Sheets Nanocomposites with Highly Enhanced Visible Light Photocatalytic Activity and Stability, *Appl. Catal., B*, 2013, **132–133**, 45–53.
- 53 A. V. Murugan, T. Muraliganth and A. Manthiram, Rapid, Facile Microwave-Solvothermal Synthesis of Graphene

- Nanosheets and Their Polyaniline Nanocomposites for Energy Storage, *Chem. Mater.*, 2009, **21**, 5004–5006.
- 54 Y. R. Jiang, H. P. Lin, W. H. Chung, Y. M. Dai, W. Y. Lin and C. C. Chen, Controlled hydrothermal synthesis of $\text{BiO}_x\text{Cl}_y/\text{BiO}_m\text{I}_n$ composites exhibiting visible-light photocatalytic degradation of crystal violet, *J. Hazard. Mater.*, 2015, **283**, 787–805.
- 55 F. Dong, Y. Sun, M. Fu, Z. Wu and S. C. Lee, Room Temperature Synthesis and Highly Enhanced Visible Light Photocatalytic Activity of Porous BiOI/BiOCl Composites Nanoplates Microflowers, *J. Hazard. Mater.*, 2012, **219–220**, 26–34.
- 56 D. Chen, H. Feng and J. Li, Graphene Oxide: Preparation, Functionalization, and Electrochemical Applications, *Chem. Rev.*, 2012, **112**, 6027–6053.
- 57 D. Yang, A. Velamakanni, G. Bozoklu, S. Park, M. Stoller, R. D. Piner, S. Stankovich, I. Jung, D. A. Field and C. A. Ventrice, Chemical Analysis of Graphene Oxide Films after Heat and Chemical Treatments by X-ray Photoelectron and Micro-Raman Spectroscopy, *Carbon*, 2009, **47**, 145–152.
- 58 L. Lin, S. Yuan, J. Chen, L. Wang, J. Wan and X. Lu, Treatment of chloramphenicol-contaminated soil by microwave radiation, *Chemosphere*, 2010, **78**, 66–71.
- 59 A. Chatzitakis, C. Berberidou, I. Paspaltsis, G. Kyriakou, T. Sklaviadis and I. Poullos, Photocatalytic degradation and drug activity reduction of chloramphenicol, *Water Res.*, 2008, **42**, 386–394.
- 60 K. Ishibashi, A. Fujishima, T. Watanabe and K. Hashimoto, Detection of Active Oxidative Species in TiO_2 Photocatalysis Using the Fluorescence Technique, *Electrochem. Commun.*, 2000, **2**, 207–210.
- 61 S. T. Huang, Y. R. Jiang, S. Y. Chou, Y. M. Dai and C. C. Chen, Synthesis, characterization, photocatalytic activity of visible-light-responsive photocatalysts $\text{BiO}_x\text{Cl}_y/\text{BiO}_m\text{Br}_n$ by controlled hydrothermal method, *J. Mol. Catal. A: Chem.*, 2014, **391**, 105–120.
- 62 C. Nasr, K. Vinodgopal, L. Fisher, S. Hotchandani, A. K. Chattopadhyay and P. V. Kamat, Environmental Photochemistry on Semiconductor Surfaces. Visible Light Induced Degradation of a Textile Diazo Dye, Naphthol Blue Black, on TiO_2 Nanoparticles, *J. Phys. Chem.*, 1996, **100**, 8436–8442.
- 63 X. Xiao, R. Hao, M. Liang, X. Zuo, J. Nan, L. Li and W. Zhang, One-pot solvothermal synthesis of three-dimensional (3D) BiOI/BiOCl composites with enhanced visible-light photocatalytic activities for the degradation of bisphenol-A, *J. Hazard. Mater.*, 2012, **233–234**, 122–130.
- 64 N. M. Dimitrijevic, B. K. Vijayan, O. G. Poluektov, T. Rajh, K. A. Gray, H. He and P. Zapol, Role of Water and Carbonates in Photocatalytic Transformation of CO_2 to CH_4 on Titania, *J. Am. Chem. Soc.*, 2011, **133**, 3964–3971.
- 65 H. Y. Mao, S. Laurent, W. Chen, O. Akhavan, M. Imani, A. A. Ashkarran and M. Mahmoudi, Graphene: Promises, Facts, Opportunities, and Challenges in Nanomedicine, *Chem. Rev.*, 2013, **113**, 3407–3424.
- 66 Y. Wang, W. Wang, H. Mao, Y. Lu, J. Lu, J. Huang, Z. Ye and B. Lu, Electrostatic Self-Assembly of BiVO_4 -Reduced Graphene Oxide Nanocomposites for Highly Efficient Visible Light Photocatalytic Activities, *ACS Appl. Mater. Interfaces*, 2014, **6**, 12698–12706.
- 67 X. Bai, L. Wang and Y. Zhu, Visible Photocatalytic Activity Enhancement of ZnWO_4 by Graphene Hybridization, *ACS Catal.*, 2012, **2**, 2769–2778.
- 68 S. Shenawi-Khalil, V. Uvarov, S. Fronton, I. Popov and Y. Sasson, A Novel Heterojunction $\text{BiOBr}/\text{Bismuth Oxyhydrate}$ Photocatalyst with Highly Enhanced Visible Light Photocatalytic Properties, *J. Phys. Chem. C*, 2012, **116**, 11004–11012.
- 69 D. L. Jiang, L. I. Chen, J. J. Zhu, M. Chen, W. D. Shi and J. M. Xie, *Dalton Trans.*, 2013, **42**, 15726–15734.
- 70 H. J. Fan, C. S. Lu, W. L. W. Lee, M. R. Chiou and C. C. Chen, Mechanistic pathways differences between P25-TiO_2 and Pt-TiO_2 mediated CV photodegradation, *J. Hazard. Mater.*, 2011, **185**, 227–235.
- 71 C. C. Chen, F. D. Mai, K. T. Chen and C. S. Lu, Photocatalyzed *N*-de-methylation and degradation of crystal violet in titania dispersions under UV irradiation, *Dyes Pigm.*, 2007, **75**, 434–442.